

## SUPPLEMENTARY INFORMATION

# Enhanced electrical properties of BNKT-BMN lead-free ceramics by $\text{CaSnO}_3$ doping and their bioactive properties

Lalita Tawee,<sup>a</sup> Narongdetch Boothrawong,<sup>a</sup> Suwanan Thammarong,<sup>b</sup> Phanrawee Sriprapha,<sup>a</sup> Waraporn Boontakam,<sup>a</sup> Denis Russell Sweatman<sup>a,c,d</sup>, Nopakarn Chandet,<sup>d</sup> Chamnan Randorn,<sup>d</sup> Gobwute Rujijanagul,<sup>\*ace</sup>

<sup>a</sup>Department of Physics and Materials Science, Faculty of Science, Chiang Mai University, Chiang Mai 50200, Thailand

<sup>b</sup>State Key Laboratory of Structure Analysis for Industrial Equipment, Department of Engineering Mechanics, Dalian University of Technology, Dalian 116024, China

<sup>c</sup>Office of Research Administration, Chiang Mai University, Chiang Mai 50200, Thailand

<sup>d</sup>Materials Science Research Center, Faculty of Science, Chiang Mai University, Chiang Mai 50200, Thailand

<sup>e</sup>Department of Chemistry, Faculty of Science, Chiang Mai University, Chiang Mai 50200, Thailand

<sup>f</sup>Multidisciplinary and Interdisciplinary School, Chiang Mai University, Chiang Mai 50200, Thailand

### Figure of Contents

	Pages
Fig. S1 (a) Tolerance factor ( $t$ ) and $c/a$ as a function of $\text{CaSnO}_3$ content (Inset: $t$ vs. $c/a$ ) and (b) $r_{A_{\text{site}}}$ , $r_{B_{\text{site}}}$ versus $\text{CaSnO}_3$ content.	2
Fig. S2 Plots of the inverse dielectric permittivity ( $1/\epsilon_r$ ) as a function of temperature for the $(1-x)[0.99\text{BNKT}-0.01\text{BMN}]-x\text{CSO}$ ceramics: (a) $x = 0.00$ , (b) $x = 0.02$ , and (c) $x = 0.04$ .	3
Fig. S3 (a) $W_{\text{rec}}$ , (b) $W_{\text{loss}}$ , and (c) $\Delta P$ values versus electric field.	4
Fig. S4 Temperature dependence of $P-E$ hysteresis loops of $(1-x)[0.99\text{BNKT}-0.01\text{BMN}]-x\text{CSO}$ ceramics.	4
Fig. S5 Schematic diagram showing the dip coating process.	6
Fig. S6 EDS mapping analysis that corresponding with Fig.11(b) of the apatite layer after the samples were immersion in SBF for 30 days.	6

### Table of Contents

	Pages
Table S1 Dielectric properties of $(1-x)[0.99\text{BNKT}-0.01\text{BMN}]-x\text{CSO}$ ceramics.	2
Table S2 Ferroelectric and energy storage properties of $(1-x)[0.99\text{BNKT}-0.01\text{BMN}]-x\text{CSO}$ ceramics.	3
Table S3 Piezoelectric properties of $(1-x)[0.99\text{BNKT}-0.01\text{BMN}]-x\text{CSO}$ ceramics at RT.	5
Table S4 Mechanical properties of the $(1-x)[0.99\text{BNKT}-0.01\text{BMN}]-x\text{CSO}$ ceramics.	5

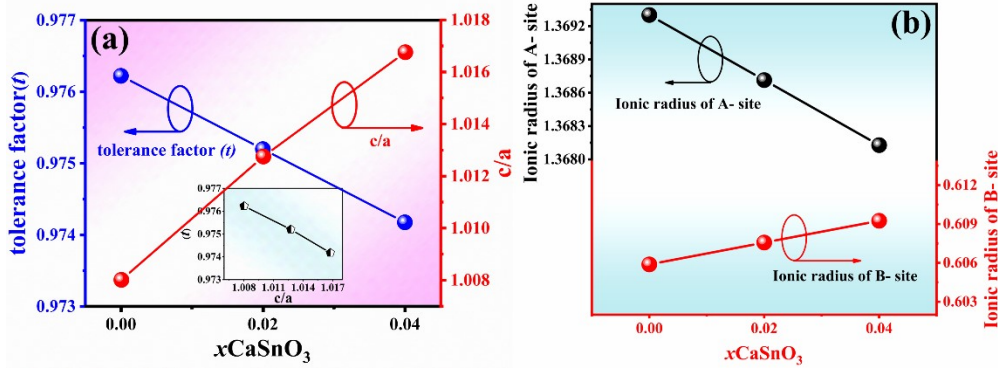


**Fig. S1** (a) Tolerance factor ( $t$ ) and  $c/a$  as a function of  $\text{CaSnO}_3$  content (Inset:  $t$  vs.  $c/a$ ) and (b)  $r_{A\text{-site}}$ ,  $r_{B\text{-site}}$  versus  $\text{CaSnO}_3$  content.

The tolerance factor ( $t$ ) of the ceramics system was calculated based on the equations:

$$t = \frac{r_{A\text{-site}} + r_{B\text{-site}}}{\sqrt{2}(r_{B\text{-site}} + r_{\text{O}})} \quad (\text{S1})$$

$$r_{A\text{-site}} = (1-x) \left[ [(0.99)(0.5)r_{\text{Bi}^{3+}}] + [(0.01)r_{\text{Bi}^{3+}}] + [(0.99)(0.8)(0.5)r_{\text{Na}^+}] + [(0.99)(0.2)(0.5)r_{\text{K}^+}] \right] + x(r_{\text{Ca}^{2+}}) \quad (\text{S2})$$

$$r_{B\text{-site}} = (1-x) \left[ (0.01) \left( \frac{2}{3} \right) (r_{\text{Mg}^{2+}}) \right] + \left[ (0.01) \left( \frac{1}{3} \right) (r_{\text{Nb}^{5+}}) \right] + [(0.99)(r_{\text{Ti}^{4+}})] + x(r_{\text{Sn}^{4+}}) \quad (\text{S3})$$

, where  $r_{A\text{-site}}$ ,  $r_{B\text{-site}}$  and  $r_{\text{O}}$  represent the radii of the A-site, B-site ions, and oxygen ion of the studied system, respectively. Furthermore,  $r_{\text{Bi}^{3+}}$ ,  $r_{\text{Na}^+}$ ,  $r_{\text{K}^+}$ ,  $r_{\text{Ca}^{2+}}$ ,  $r_{\text{Mg}^{2+}}$ ,  $r_{\text{Nb}^{5+}}$ ,  $r_{\text{Ti}^{4+}}$  are radii of the Bi, Na, K, Ca, Mg, Nb, and Ti ions, respectively. The result for the  $t$  value calculation is shown in Fig. S1(a). Ionic radius of A-site and B-site ions as a function of  $\text{CaSnO}_3$  content are displayed in Fig. S1(b). The ionic radii of A-site and B-site ions increased with  $\text{CaSnO}_3$ . The  $t$  value also increased with increasing CSO content. However, the  $t$  value was found in a range 0.9742-0.9762, which is in a range of the stable perovskite structure ( $0.880 < t < 1.090$ ). Thus, the investigated composition belongs to the stable perovskite structure. This corresponds to the XRD result where the investigated samples exhibited the pure phase. Fig. S1 also presents the  $c/a$  value as a function of  $\text{CaSnO}_3$  content. The  $c/a$  value slightly increased with increasing CSO content. Moreover, the  $t$ -value had a decreasing trend with the  $c/a$  value (inset of Fig. S1(a)). The obtained results, therefore, indicated that  $\text{CaSnO}_3$  additive promoted the lattice distortion of the studied ceramic system.

**Table S1** Dielectric properties of  $(1-x)[0.99\text{BNKT}-0.01\text{BMN}]-x\text{CSO}$  ceramics.

$x$	$\varepsilon_r^a$	$\tan \delta^a$	$\varepsilon_{r\text{max}}$	$\tan \delta^b$	$T_m$ (°C)	$T_B$ (°C)	$\Delta(T_B - T_m)$	$\Delta\varepsilon_{1\text{kHz}} - \varepsilon_{1\text{MHz}}$
0.00	1412	0.0415	4241	0.0398	326	439	113	838.79
0.02	1288	0.0402	3236	0.0303	317	433	116	794.09
0.04	1178	0.0336	2765	0.0385	313	431	118	503.38

- <sup>a</sup> Dielectric loss ( $\tan \delta$ ) measured at RT and 1 kHz.  
<sup>b</sup> Dielectric loss ( $\tan \delta$ ) measured at  $T = T_m$  and 1 kHz.

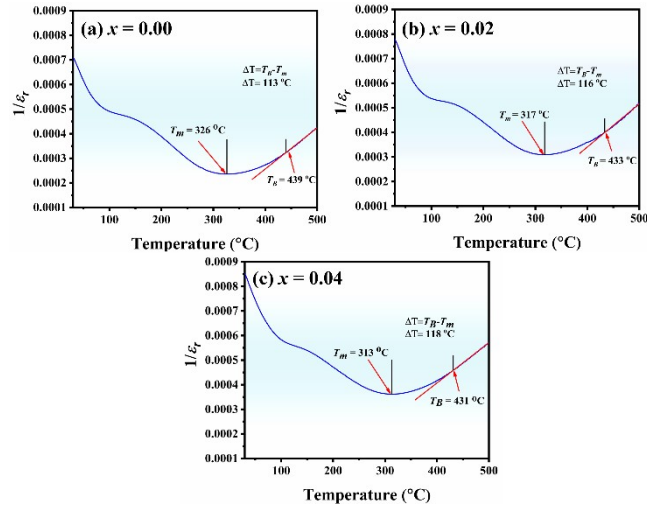


**Fig. S2** Plots of the inverse dielectric permittivity ( $1/\epsilon_r$ ) as a function of temperature for the  $((1-x)[0.99\text{BNKT}-0.01\text{BMN}]-x\text{CSO})$  ceramics: (a)  $x = 0.00$ , (b)  $x = 0.02$ , and (c)  $x = 0.04$ .

The Burns temperature ( $T_B$ ), the temperature at which the dielectric constant begins to deviate from the Curie-Weiss law, was obtained from the plots of the inverse dielectric permittivity ( $1/\epsilon_r$ ) as a function of temperature (Fig. S2). Normally, relaxors subsist as a nonpolar paraelectric phase at a higher temperature which is similar to the paraelectric phase of ferroelectrics. However, throughout the cooling cycle, they undergo a transformation and form an ergodic relaxor (ER) state at  $T_B$ , which is the onset point of polarization in relaxors [S1]. In this work, the  $T_B$  decreased with increasing the CSO content. Furthermore, the deviation from the Curie-Weiss law was evaluated from  $\Delta T$  as the following equation shows [S2]:  $\Delta T = T_B - T_m$ . It was found that the  $\Delta T$  increased with increasing CSO content, indicating the diffused phase transition behavior was enhanced [S2].

**Table S2** Ferroelectric and energy storage properties of  $(1-x)[0.99\text{BNKT}-0.01\text{BMN}]-x\text{CSO}$  ceramics.

$x$	$P_{\max}^{(a)}$ ( $\mu\text{C cm}^{-2}$ )	$P_r^{(a)}$ ( $\mu\text{C cm}^{-2}$ )	$P_{\max}-P_r^{(a)}$ ( $\mu\text{C cm}^{-2}$ )	$E_c^{(a)}$ ( $\text{kV cm}^{-1}$ )	$W_{\text{rec}}^{(a)}$ ( $\text{mJ cm}^{-3}$ )	$\eta^{(a)}$ (%)	$W_{\text{rec}}^{(b)}$ ( $\text{mJ cm}^{-3}$ )	$\eta^{(b)}$ (%)	$E_B^{(a)}$ ( $\text{kV cm}^{-1}$ )	$E_B^{(b)}$ ( $\text{kV cm}^{-1}$ )
0.00	39.98	27.05	12.93	24.16	320	19.68	306	71.55	40	60
0.02	37.31	16.07	21.24	20.36	781	42.99	1071	59.69	60	60
0.04	28.36	8.77	19.59	17.65	597	43.61	849	59.56	60	60

<sup>(a)</sup> The data obtained at RT.

<sup>(b)</sup> The data obtained at 150 °C.

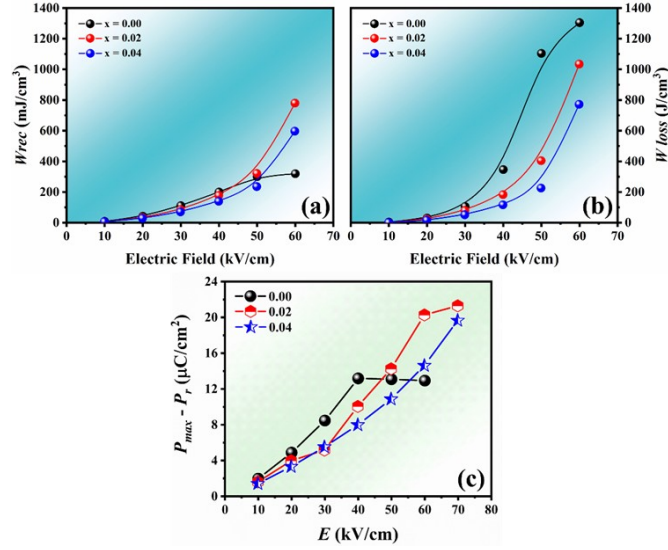


**Fig. S3** (a)  $W_{rec}$ , (b)  $W_{loss}$ , and (c)  $\Delta P$  values versus electric field.

**Table S2** lists ferroelectric and energy storage properties of the studied ceramics. Furthermore, values of  $W_{rec}$ ,  $W_{loss}$ , and  $\Delta P (=P_{max}-P_r)$  as a function of electric field are displayed in **Fig. S3**. The increasing rate of  $W_{loss}$  value under the electric field was higher than that of the rate of  $W_{rec}$  value, thus the  $\eta$  value decreased with the electric field (**Fig. 6(b)**). In addition, the  $\Delta P$  tended to increase with the electric field, resulting in an increasing trend of the  $W_{rec}$  value with the electric field (**Fig. 6(a)**).

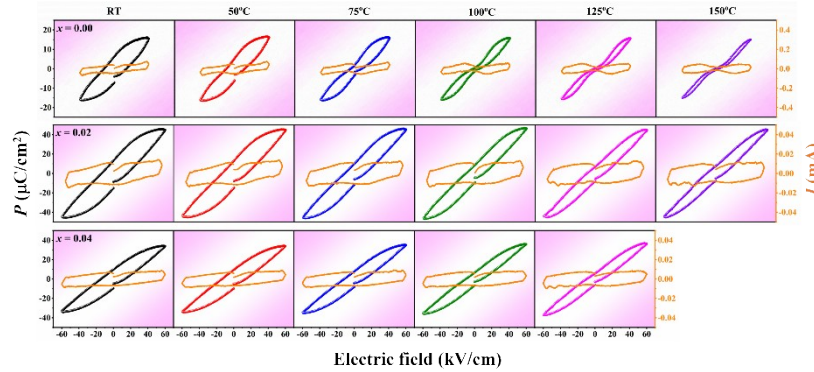


**Fig. S4** Temperature dependence of  $P-E$  hysteresis loops of  $(1-x)[0.99\text{BNKT}-0.01\text{BMN}]-x\text{CSO}$  ceramics.

The  $P-E$  hysteresis loops of the  $(1-x)[0.99\text{BNKT}-0.01\text{BMN}]-x\text{CSO}$  ceramics as a function of temperature are shown in **Fig. S4**. The  $P-E$  loops became more pinched and slimmer with increasing CSO content. The onset temperature for the constrictive loop tended to shift down to RT with CSO content, which is consistent with the trend of  $T_{F-R}$ . Based on the obtained results, both chemical composition and temperature affected the lattice deformation and disturbance of the FE long-range order, resulting in an effect on the ferroelectric properties.

**Table S3** Piezoelectric properties of (1-x)[0.99BNKT-0.01BMN]-xCSO ceramics at RT.

x	$S_{max}$ (%)	$S_{neg}$ (%)	$d_{33}^*$ (pm V <sup>-1</sup> )	$d_{33}$ (pC N <sup>-1</sup> )	$g_{33}$ (10 <sup>-3</sup> Vm N <sup>-1</sup> )	FoM (pm <sup>2</sup> N <sup>-1</sup> )
0.00	0.20	-0.06	342	188	15.04	2.83
0.02	0.30	-0.01	505	77	6.75	0.52
0.04	0.28	0.00	467	65	6.23	0.40

The piezoelectric characteristics of the studied samples are displayed in [Table S3](#). The maximum  $S_{max}$  and  $d_{33}^*$  were found for the  $x = 0.02$  samples, while  $d_{33}$ ,  $g_{33}$ , and  $FoM$  decreased with CSO content, due to the CSO promoting the transformation of FE to ER phase.

**Table S4** Mechanical properties of the (1-x)[0.99BNKT-0.01BMN]-xCSO ceramics.

x	$H_v$ (GPa)	$H_k$ (GPa)	$E_m$ (GPa)	$K_{IC}$ (MPa.m <sup>1/2</sup> )
0.00	5.93	5.51	133	1.04
0.02	6.01	5.57	134	0.97
0.04	6.11	5.66	135	0.93

Mechanical properties of the studied ceramics are listed in [Table S4](#). The CSO additive increased the mechanical characteristics such as hardness and elastic modulus of the examined ceramics.

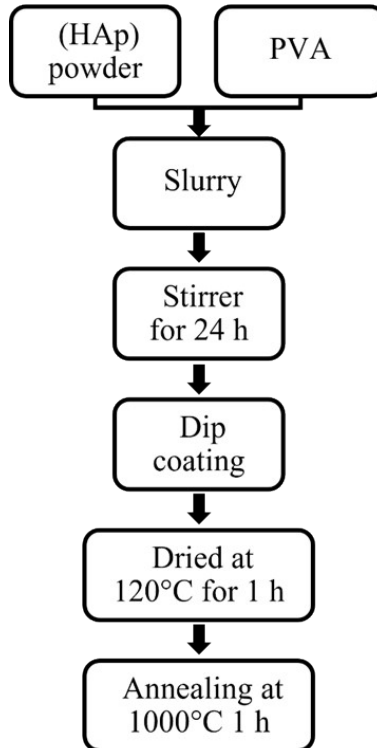


**Fig. S5** Schematic diagram showing the dip coating process.

The schematic diagram of the dip coating process is presented in Fig. S5. A slurry for the coating was prepared by mixing 2.0 g of hydroxyapatite (HAp) powder and 0.2 g of polyvinyl alcohol with 5 cc of distilled water. The slurry was stirred using a magnetic stirrer for 24 h at room temperature. For the dip coating, the 0.02 samples were drawn up at a speed of  $1 \text{ mm s}^{-1}$ . The coated samples were then dried at  $120 \text{ }^\circ\text{C}$  for 1 h to form a white-coated film, followed by annealing at  $1000 \text{ }^\circ\text{C}$  for  $1 \text{ h}$  using a heating and cooling rate of  $10 \text{ }^\circ\text{C min}^{-1}$  [S3]. The microstructure of the uncoated and coated samples was examined using the SEM. To test the bioactivity of the coated samples, an in vitro experiment was carried out using a simulated bodily fluid (SBF) assay. For this experiment, the samples were immersed in an SBF solution at a pH of 7.4 and a temperature of  $37 \pm 0.5 \text{ }^\circ\text{C}$  for 15 days.

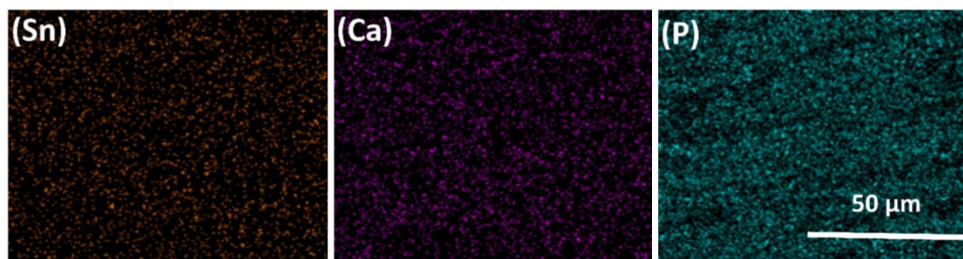


Fig.S6 EDS mapping analysis that corresponding with Fig.11(b) of the apatite layer after the samples were immersion in SBF for 30 days.

The EDS analysis results of the apatite layer formed after immersing the sample in SBF for 30 days are presented in Fig. S6, which corresponds to the surface of the samples shown in Fig. 11(b). The EDS analysis revealed the creation of apatite layers, as indicated by the presence of Ca and P elements. Particularly, samples not submerged in SBF should not include P, which is a component of the apatite layer. Based on EDS analysis result and Fig. 11(a), bone-like apatite layers developed after immersing the samples in SBF.

## References for supplementary information

- S1 S.K. Gupta, R.M. Quade, B. Gibbons, P. Mardilovich and D.P. Cann, *J. Appl. Phys.*, 2020, **127**, 074104.
- S2 R. Kang, Z. Wang, X. Lou, W. Liu, P. Shi, X. Zhu, X. Guo, S. Li, H. Sun, L. Zhang and Q. Sun, *Chem. Eng. J.*, 2021, **410**, 128376.
- S3 R. Asmawi, M.H. Ibrahim, A. M. Amin, N. Mustafa and Z. Noranai, *Mater. Sci. Eng.*, 2017, **226**, 012179.